An experimental and numerical study of the high cycle multiaxial fatigue strength of titanium lattice structures produced by Selective Laser Melting (SLM)

Khalil Refai, Charles Brugger, Marco Montemurro, Nicolas Saintier

Version of Record: https://www.sciencedirect.com/science/article/pii/S0142112320301547
Manuscript_f12ab7c63e1680f6ea74d76045527c27

An experimental and numerical study of the high cycle multiaxial fatigue strength of titanium lattice structures produced by Selective Laser Melting (SLM)

Khalil Refai[a], Charles Brugger[a,*], Marco Montemurro[a], Nicolas Saintier[a]

[a] *Arts et Metiers Institute of Technology, University of Bordeaux, CNRS, Bordeaux INP, INRAE, I2M Bordeaux, F-33400 Talence, France*

Abstract

A numerical approach is proposed to assess the high cycle fatigue (HCF) strength of periodic cellular structures produced by Selective Laser Melting under multiaxial loads. The model is based on a general numerical homogenisation scheme and an explicit description of the Elementary Cell (EC) combined to an extreme values analysis making use of a fatigue indicator parameter based on Crossland's criterion. This method is applied to 33 EC topologies.
In addition, geometric discrepancy and surface roughness are experimentally characterised and considered in the numerical model using three methods which are compared to the experimental HCF strength.

Keywords: Additive manufacturing, Lattice structures, Homogenisation, Multiaxial high-cycle fatigue, Extreme Value Theory.

Nomenclature

R	Fillet radius
V_{EC}	Overall volume of the EC
V_{EFF}	Actual volume of the EC
Ω	Sphere diameter
$\mathbf{S}$	Compliance tensor
$\varepsilon^{\mathbf{0}}_{\mathbf{k}}$	Mesoscopic average strain tensors
$\overline{\boldsymbol{\sigma}}(t)$	Macroscopic cyclic loads
$\overline{\rho}$	Relative density $\frac{V_{\mathrm{EFF}}}{V_{\mathrm{EC}}}$
$\overline{\sigma_0}$	Amplitude of the arbitrary macroscopic initial applied load
$\overline{\sigma}_D$	Macroscopic fatigue strength

*Corresponding author. Tel.: +33 5 56 84 53 65.
Email address: charles.brugger@ensam.eu (Charles Brugger)

σ^* FIP value obtained for σ_0.

d_{CAD} Diameter of the CAD cross-section

EC Elementary Cell

FIP Fatigue Indicator Parameter

TPMS Triply Periodic Minimal Surface

1. Introduction

In the last two decades, a strong effort has been put on the development of additive layer manufacturing technology because of the advantages it offers including design freedom, high precision, and the ability to produce parts directly from a CAD model. It makes possible the production of periodic cellular structures, which exhibit a unique combination of properties, including lightness, high stiffness and high strength. The macroscopic elastic and fatigue behaviours of these structures depend on several factors such as cell topology, material and manufacturing process characteristics, as well as loading conditions. By modifying the elementary cell (EC) topology and the relative density at the mesoscopic scale (the scale of the EC, 4 mm in this study), one can fulfill the desired requirements at the macroscopic one (the scale of the specimen).

Only a few studies focusing on the High Cycle Fatigue (HCF) resistance of periodic cellular structures which aim at understanding the relationship between the elementary cell (EC) geometrical parameters and its fatigue strength are available in the literature [1–14]. In particular, Yavari *et al.* [12] observed that the fatigue strength of the SLM Ti-6Al-4V porous structures under compressive loads decreases with the relative density. In [13], three types of Ti-6Al-4V lattice structures with cubic, octahedral (noted G7) and rhombic dodecahedron ECs were fabricated by Zhao *et al.* using the EBM technique. The results clearly proved that the fatigue strength under compression is strongly influenced by the geometry of the EC. In [14], Hedayati *et al.* analysed (numerically) the HCF resistance of three different EC geometries, i.e. diamond, rhombic dodecahedron and truncated cuboctahedron, under uniaxial cyclic compressive load while varying the relative density values from 0.1 to 0.3. A failure event-based algorithm as well as a stress-life approach were used to simulate the fatigue failure within the bulk material of the lattice. Results showed that fatigue strength and cycles to failure were related according to a standard power law. The coefficient of the power function depended upon the relative density, the geometrical parameters of the lattice and the fatigue properties of the bulk material, while the exponent was only affected by the first two quantities. Results also indicated that the crack onset occurs at an angle of 45° with respect to the load direction.

In general, fatigue tests of periodic cellular structures is a costly and time consuming process. Moreover, as mentioned above, there are many factors affecting it. Consequently, it is very useful to implement dedicated numerical models in order to investigate the influence of each factor on the HCF strength of the structure before manufacturing and testing the specimens. Accordingly, the aim of this work is to provide a deeper insight into the influence of the EC topology and its relative density on the fatigue strength under multiaxial high-cycle loads. To properly apply the multiaxial loading conditions to the EC at the mesoscopic scale, a numerical homogenisation scheme relying on the strain energy of periodic media [15–17] has been used. In this background, the numerical simulations are conducted at different scales, i.e. mesoscopic scale (that of the EC) and macroscopic

one (the scale of the specimen where the periodic cellular structure is modelled as an equivalent homogeneous anisotropic material).

In order to obtain optimised and manufacturable structures, it is necessary to formally define the manufacturability of candidate EC geometries and characterise the related fatigue strength. EC topologies of engineering relevance are fabricated, microstructure characterisation and surface analysis are carried out respectively by Optical Microscope (OM), Scanning Electron Microscope (SEM) and micro-Computed Tomography (μCT). Beside experimental investigation, numerical simulations on a dedicated finite element (FE) model of the lattice are conducted using a virtual generated rough surfaces. Based on extreme values statistics of the Crossland's equivalent stress, a methodology is proposed to take into account for the effect of the surface roughness on the HCF strength.

The paper is organised as follows. Elementary Cells geometries considered in this study are presented in Section 2. Section 3 presents the material and the experimental campaign of analyses aiming at assessing the geometric discrepancies and the influence of the surface roughness on the fatigue strength of the structures. The general numerical strategy used to investigate the fatigue strength of the EC together with the multiaxial fatigue criterion employed in this work and the fundamentals of the extreme value theory (EVT) are presented in Section 4. Numerical and experimental results are illustrated and discussed in Sections 5 and 5.5. Finally, Section 6 ends the paper with some conclusions and prospects.

2. Cells geometries

This work aims to assess and compare the fatigue strength of various periodic cellular structures made of Ti-6Al-4V gathered in three main classes. The "lattice" class includes 18 lattice structures whose EC is an arrangement of struts, as show in Fig. 1 [18]. "Thin-walled TPMS" and "Skeletal TMPS" classes include ECs obtained from triply periodic minimal surfaces (TPMS). The 9 "Thin-walled TPMS" (Fig. 2(a)) [19, 20] are generated by applying a constant thickness to an implicit surface (see (1) for examples). The 6 "Skeletal TPMS" structures (Fig. 2(b)) are built by boolean operations on ECs from the other two classes.

$$\begin{cases} 0 = \cos(k_x x) + \cos(k_y y) + \cos(k_z z) - t, & \text{Schwarz,} \\ 0 = \cos(k_x x)\sin(k_y y) + \cos(k_y y)\sin(k_z z) + \cos(k_z z)\sin(k_x x) - t, & \text{Gyroid,} \\ 0 = 2(\cos(k_y y)\cos(k_z z) + \cos(k_x x)\cos(k_y y) + \cos(k_x x)\cos(k_z z)) - \\ \qquad (\cos(2k_x x) + \cos(2k_y y) + \cos(2k_z z)) - t, & \text{IWP,} \\ 0 = 3(\cos(k_x x) + \cos(k_y y) + \cos(k_z z)) + 4\cos(k_x x)\cos(k_y y)\cos(k_z z), & \text{Neovius.} \end{cases} \tag{1}$$

where k_i are defined as:

$$k_i = 2\pi\frac{n_i}{L},\ i = x, y, z, \tag{2}$$

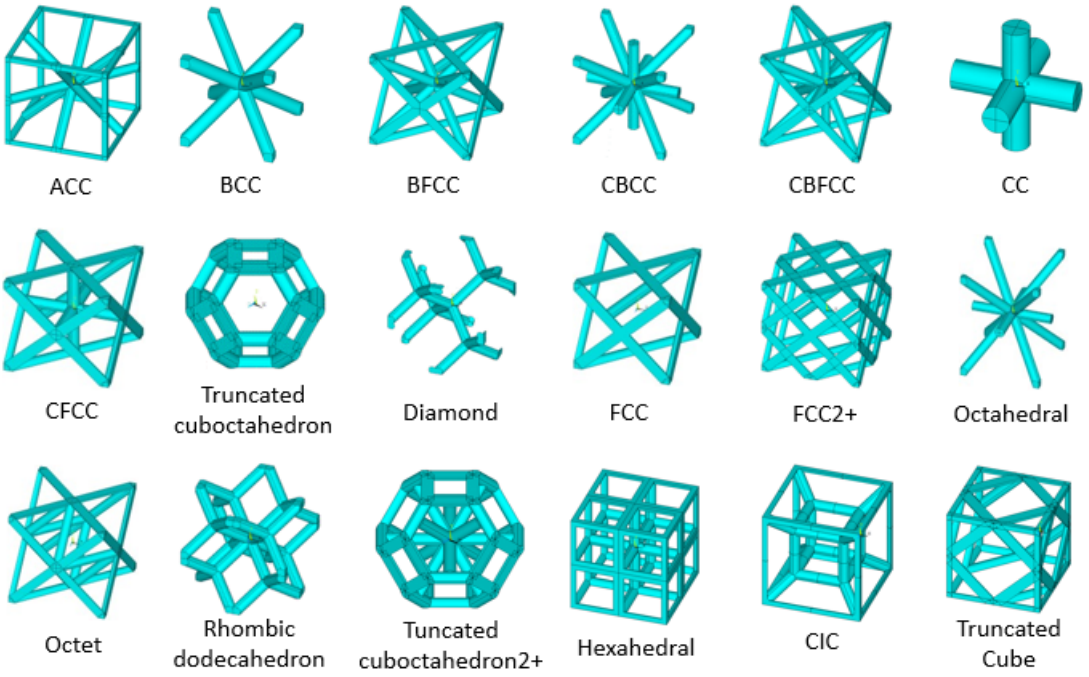

Figure 1: Lattice structures.

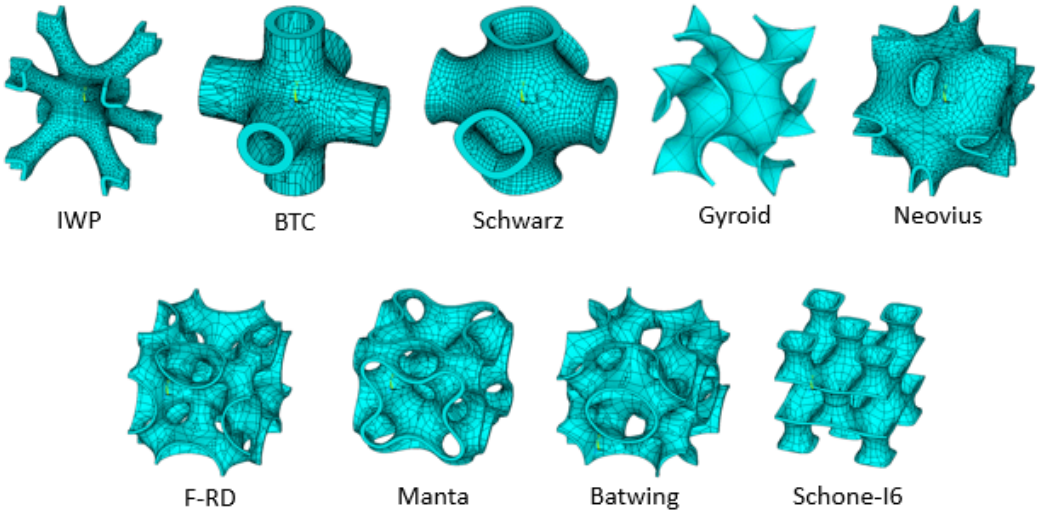

(a) Thin-walled TPMS

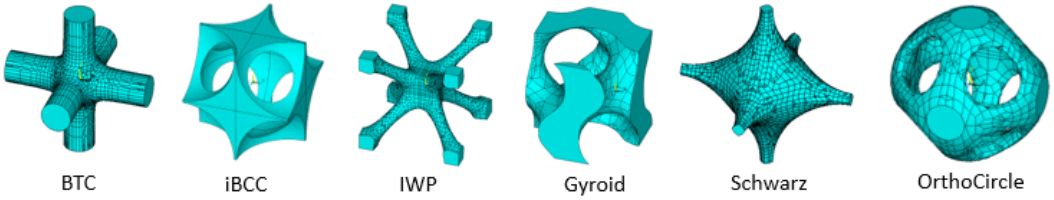

(b) Skeletal-TPMS

Figure 2: (a) Thin-walled and (b) skeletal TPMS structures.

Regardless of its topology, each EC fits in a parallelepiped whose overall volume is

$V_{\text{EC}} = 8a_1a_2a_3$, as illustrated in Fig. 3. In this study, since the objective is to identify ECs exhibiting good fatigue strength under any multiaxial loading, we chose not to favour any direction, neither through topology nor dimensions. We will then consider $a_1 = a_2 = a_3 = a$.

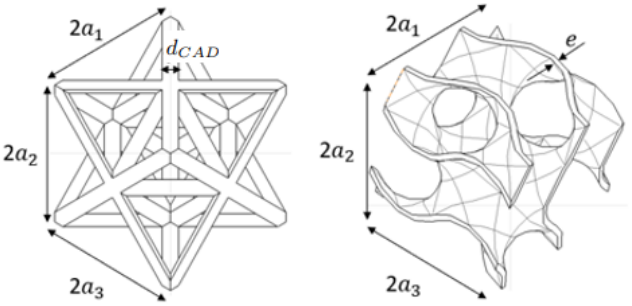

(a) Octet EC (b) Gyroid EC

Figure 3: Examples of EC topologies and related geometric parameters: strut diameter d_{CAD} and wall thickness e.

In addition to its topology and size a, each EC requires geometric parameters to be fully described. For instance, since lattice structures are composed of struts, the diameter of the cross-section d_{CAD} must be specified, whilst thin-walled TPMS require the value of the constant thickness applied to the implicit surface.

3. Material and methods

3.1. SLM processing

Specimens were manufactured using a SLM280HL machine. The material is a Ti-6Al-4V alloy whose chemical composition is illustrated in Table 1. The powder has a spherical morphology with a particle size distribution of 20-63 μm.

Elem	Ti	Al	V	C	O	N	Fe	H	Autres
%	Bal.	5.50-6.50	3.50-4.50	0.08	0.13	0.03	0.25	0.0125	0.10

Table 1: Ti-6Al-4V (grade 5) powder chemical composition according to AFNOR L14-601.

The standard process parameters were applied, see Table 2, a back-and-forth "stripes" scanning strategy and argon was used as a protective atmosphere.

$P\ (W)$	$h\ (mm)$	Focal offset (mm)	$v\ (mm/s)$	$t_{layer}\ (\mu m)$
400	0.12	2	710	30

Table 2: SLM processing parameters: P: laser power, h: hatch spacing, v: scan speed and t_{layer}: layer thickness.

3.2. Post-treatements

In order to reduce (eliminate) the tensile residual stresses and porosity, both Stress-Relieving (SR) and Hot Isostatic Pressing (HIP) post-processing treatments were conducted. The SR was conducted while specimens were still attached to the building plate, at a temperature of 640°C during four hours, whilst HIP treatment consists in applying an isostatic pressure of 1020 bars at a temperature of 920°C during two hours.

3.3. Surface roughness

When considering lattice structures manufacturing, conventional machining techniques are no longer suitable for eliminating surface defects inherited from the SLM process and resulting in stress concentration zones, which in fact correspond to favourable HCF crack initiation sites.

For small building angles, surface roughness is mostly attributed to the presence of spherical powder particles which are stuck to the melt pool but are not fully melted, see Fig. 4(a)). But for large building angles, stress concentration zones are mostly due to "plate-pile" like stacking irregularities, see Fig. 4(b)

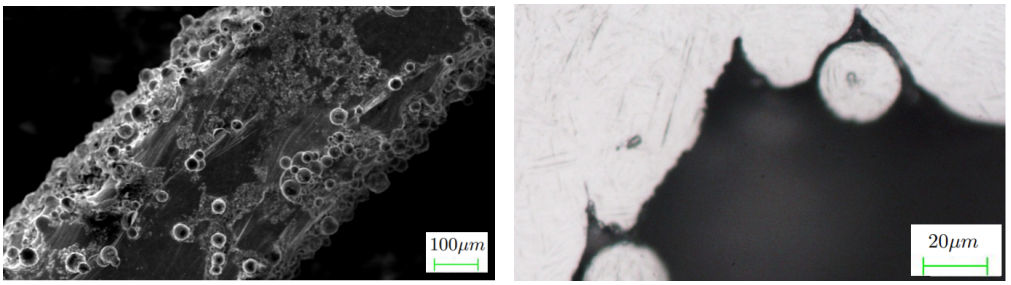

(a) (b)

Figure 4: SEM images of (a) particle adhesion and (b) notch-like defects (Building Direction is horizontal).

In order to provide a quantitative overview of the manufactured strut-based ECs morphology and to be able to numerically evaluate the effect of the surface roughness on their fatigue strength, they were inspected using OM, SEM and μCT. In particular, an octet structure was scanned using a lab-based system at PLACAMAT (UMS 3626, Pessac, France) with a Varian Paxscan detector and a microfocus X-ray tube.

The reconstructed images have a voxel size of 7 μm over 8mm in height. At each scan, the specimen was rotated in 2000 steps between 0° and 360° and an average of three images was taken at each step.

A standard filtered backprojection algorithm was used to reconstruct the final 3D image. The x-ray tube operated at electron acceleration voltages of 130 kV using a tungsten transmission target with a current of 80 μA. The spot size was equal to 3 μm during the analysis. Detailed 3D tomographic images were analysed using Avizo® software.

Following the method originally proposed by Suard *et al.* [21], the roughness of typical struts was measured from tomographic images. A series of surface profiles were extracted from 36 longitudinal sections every 5° around the strut circumference (Fig. 5). The 72 profiles obtained by this procedure for each specimen were then used to calculate the arithmetic average roughness (R_a) which is the absolute value of the profile height deviations from the mean line (l) and the maximum profile valley depth (R_v) which is the linear surface roughness parameter exhibiting the best correlation with fatigue resistance [22], both recorded within the evaluation length:

$$\begin{aligned} R_a &= \tfrac{1}{l}\int_0^l |Z(x)|dx, \\ R_v &= Z_{mean} - Z_{min}. \end{aligned} \tag{3}$$

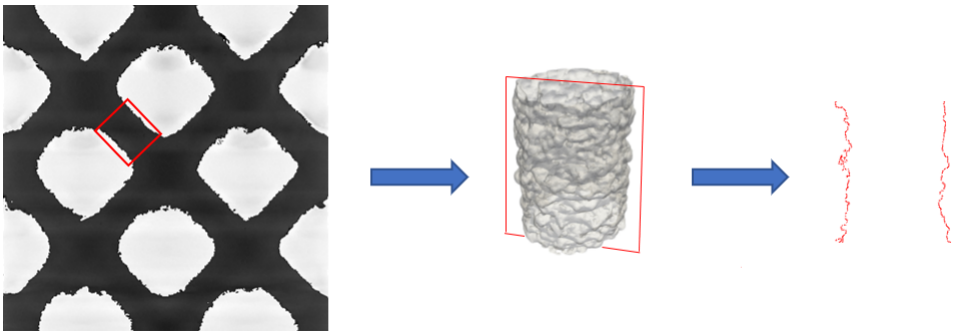

Figure 5: Schematic illustration of the methodology used to estimate roughness of the specimen surface based on X-ray CT scans.

The roughness values, in terms of arithmetical mean height and maximum valley depth, are then averaged on four quarters of the strut, each of them being composed of 18 profiles. Results obtained for three different struts orientations are given in Tables 3 and 4. Indeed, in the octet structure, struts exhibit built angles of 0°, 35.26° and 45° with respect to the building direction. The best values are obtained for upper surfaces, where dedicated "upskin" scanning parameters are used to improve roughness. As reported in the literature [23], roughness values are much larger for lower surfaces, where roughness increases as the building angle decreases. Reasons are discussed in the next subsection. For struts exhibiting a 0° built angle, R_v is about 4 times larger on the sides, and 15 times larger on the lower surface, compared to the upper surface. These ratios are almost the same for R_a.

θ	0°	35.26°	45°
R_a of the upper surface	7 μm	10 μm	11 μm
R_a of the left side surface	22 μm	19 μm	19 μm
R_a of the right side surface	21 μm	21 μm	19 μm
R_a of the lower surface	125 μm	100 μm	68 μm
R_a of the strut circumference	43.75 μm	37.5 μm	29.25 μm

Table 3: Surface roughness (R_a) variation with building angle (θ) for $d_{CAD} = 0.55mm$ and $L_{strut} = 0.9mm$.

θ	0°	35.26°	45°
R_v of the upper surface	13.3 μm	27.5 μm	27 μm
R_v of the left side	51 μm	49 μm	41 μm
R_v of the right side	55 μm	47 μm	43 μm
R_v of the lower surface	200 μm	120 μm	84 μm
R_v of the strut circumference	80 μm	61 μm	48.8 μm

Table 4: Surface roughness (R_v) variation with building angle (θ) for $d_{CAD} = 0.55mm$ and $L_{strut} = 0.9mm$.

3.4. Surface irregularities

The structures considered in this study are made of struts or walls whose dimension is close to the size of the melting pool. In addition to surface roughness, their fatigue strength then strongly depends on the presence of manufacturing defects and on the geometric

deviation from the nominal CAD geometry. This issue was addressed in two ways. First, struts with $d_{CAD} = 0.5mm$ were manufactured for various inclination angles in order to assess the surface geometric deviation. For each inclination angle, a typical cross-section was observed by optical microscopy. The shape of the cross-section (A) of the produced part is strongly affected by the strut inclination angle (θ) as shown Fig. 6.

The thermal conductivity of the powder is lower than that of the bulk. As a result, the heat flux is more likely to go through the bulk part. For high strut inclination angles, as the thermal flux is well dissipated through the strut, the circular shape of the cross-section is rather well respected, while for low values of the strut inclination angle, the thermal flux is accumulated on the down-facing side, and some powder may be unintentionally sintered. As a result the discrepancy between CAD and fabricated cross-sections increases.

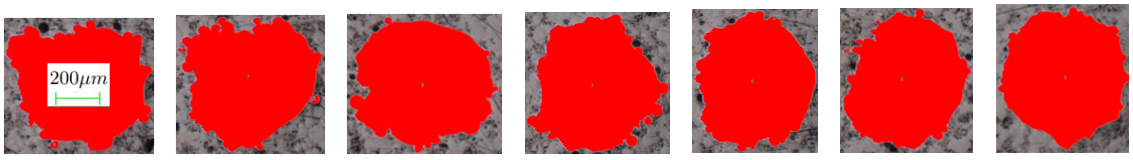

(a) 0° (b) 10° (c) 20° (d) 30° (e) 40° (f) 50° (g) 90°

Figure 6: Cross-sections of 0.5mm-diameter struts at the same scale: effect of the building angle.

The 36 longitudinal sections of the μCT scans of struts presented in the previous subsection were also analysed using the concept of "mechanically efficient material" introduced by Suard *et al.* [21]. The minimum and maximum diameters along the strut are presented Fig. 7 for each of the 36 longitudinal sections, and for a built angle of 35.26°.

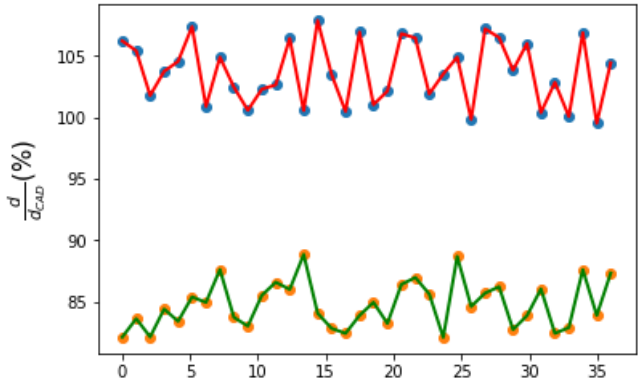

Figure 7: Minimum and maximum diameters observed on 36 longitudinal views of a 35.26° strut for $d_{CAD} = 0.55mm$ and $L_{strut} = 0.9mm$.

Averaged values (i.e., $\overline{d}_{min} = \frac{1}{36}\sum_{i=1}^{36}(d_{min})_i$, $\overline{d}_{max} = \frac{1}{36}\sum_{i=1}^{36}(d_{max})_i$ and $\overline{d}_{mean} = \frac{1}{36}\sum_{i=1}^{36}(d_{mean})_i$ for $d_{mean} = \frac{d_{max}+d_{min}}{2}$) are reported in Table 5. One can note that $\overline{d}_{max}$ is larger than the CAD diameter, due to the presence of unintentionally sintered powders. As expected, the deviation is larger for the strut at 0°, in agreement with the lower thermal flux associated to low inclination angles. On the other hand, no clear tendency is observed on $\overline{d}_{min}$. It is minimal for 35.26° building angle, with a 14% reduction of the diameter, corresponding to a 25% discrepancy regarding cross-sections area compared to CAD values. These values were measured on struts with $d_{CAD} = 0.5mm$. Absolute discrepancy values are expected to stay almost constant when strut diameter is changed,

as they are related to unintentional powder melting, and are then driven by the energy density which is constant. As a result, relative discrepancy values are expected to get better when strut diameter is increased, as one can see in Fig. 8. Observations confirmed that unintentional powder melting is restricted to down facing surfaces.

θ	$\frac{\bar{d}_{min}}{d_{CAD}}$ (mm)	$\frac{\bar{d}_{mean}}{d_{CAD}}$ (mm)	$\frac{\bar{d}_{max}}{d_{CAD}}$ (mm)	$\frac{\bar{d}_{min}}{\bar{d}_{max}}$
0°	88%	99%	110%	80%
35.26°	86.3%	95.6%	104.8%	82.3%
45°	89.4%	97.1%	104.7%	85.4%

Table 5: Strut diameters : effect of the building angle θ for $d_{CAD} = 0.55mm$.

3.5. Microstructure

Before making observations, the specimens were polished with 800 to 4000 abrasive papers grade, followed by a finishing polishing step on sheet with a non-crystallising colloidal silica suspension boosted with oxygenated water. This procedure provides mirror polished surfaces. Finally, the surfaces were attacked with Kroll reagent (4% hydrofluoric acid HF, 6% nitric acid HNO3, 90% water) to reveal the microstructure. Fig. 8 shows the microstructure of 3 struts for the same building angle of 35.26°, but for different CAD diameters (0.4 mm, 0.5 mm and 0.6 mm). Observations show an α' martensite microstructure resulting from the high cooling rate, and preliminary β grains elongated in the building direction. The columnar growth of grains is explained by the partial remelting of the previous layer. There was no major difference between the microstructures of the three struts where the β grain width varies between 80 and 150μm. These results are consistent with those available in the literature for as-build specimens [24].

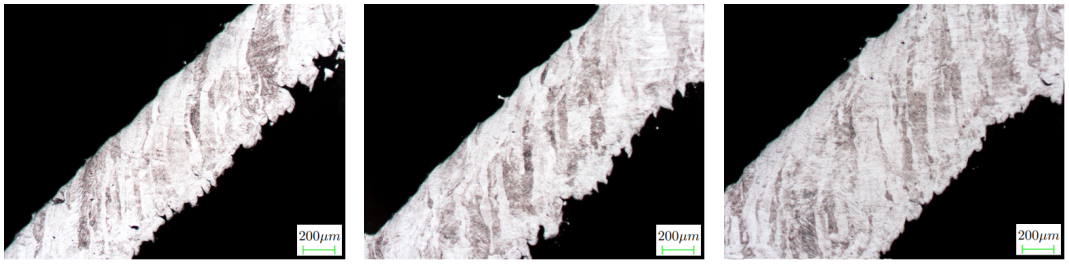

(a) 0.4 mm strut diameter (b) 0.5 mm strut diameter (c) 0.6 mm strut diameter

Figure 8: Microstructure in as-built struts for d_{CAD} = 0.4 mm (a), 0.5 mm (b), 0.6 mm (c). Building direction is vertical.

After HIP treatment (Fig. 9(a)), a lamellar microstructure is observed. The entire α' martensite phase was redissolved and the slow cooling of the HIP treatment allowed the α grains to grow and organise into a Widmanstätten structure [25] where α-lamellae thickness is between 1 and 3 μm. The colomnar ex-β grains are still distinguishable. The data processing using TSL OIM 6.1 commercial software shows that the β phase is not only oriented in the building direction, but also in the direction of the side of the part (Fig. 9(b)). This is due to the heat flow which is directed towards the edges of the struts.

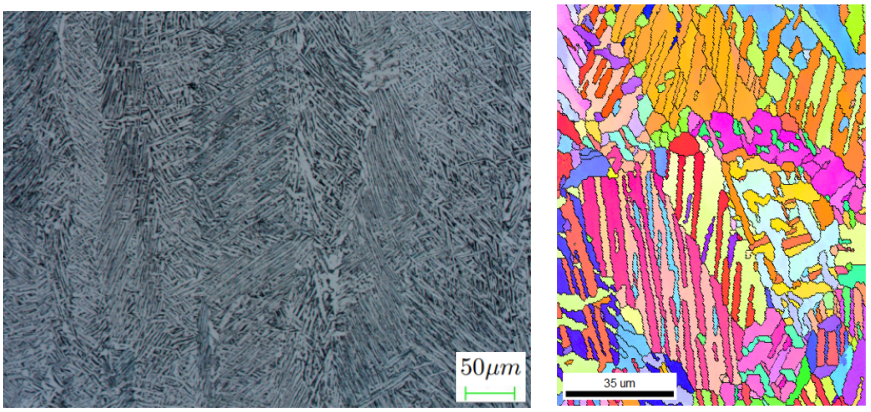

(a) (b)

Figure 9: (a) Longitudinal cross section of a HIP treated strut for a building angle 45° and $d_{CAD} = 0.55mm$. (b) Associated EBSD mapping. Building direction is vertical

3.6. HCF testing and experimental setup

Specimens were manufactured to evaluate fatigue strength of Octet and thin-walled Gyroid ECs. All specimens include a gauge section made of 4 x 4 x 4 ECs with $\overline{\rho} = 0.2$, and layers of ECs with increasing density to avoid fracture outside of the gauge, see Fig. 10 for the Octet EC. With such geometry, all specimens broke in the gauge section. Please note that all the macroscopic stresses are calculated using the external section of the specimen ($16 \times 16mm^2$), and are then reduced due to the $\overline{\rho} = 0.2$ relative density.

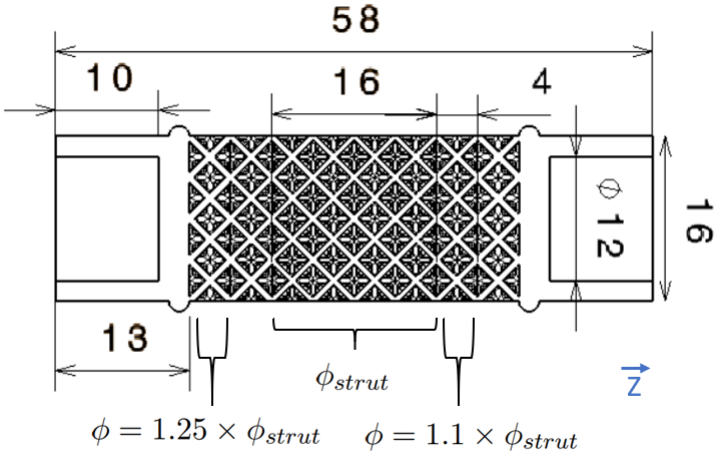

Figure 10: Octet fatigue specimen built in $\vec{Z}$ direction: gauge section made of 4 x 4 x 4 ECs surrounded by two pairs of ECs layers with increased strut diameter (dimensions in mm).

Tension-tension fatigue tests were conducted in load control using a sinusoidal waveform, with a load ratio $R_\sigma = 0.1$ to ensure that the structures were not compressed during testing, as this would likely lead to struts/walls buckling. Tests were carried out at room temperature, in air, on a Zwick resonant testing machine at 80Hz for the Octet specimens and at 100Hz for the Gyroid specimens, using the staircase method. Tests were stopped at $N_f = 10^6$ cycles or once specimens are broken in two parts.

4. Numerical strategy

After SR and HIP post-treatments, the sources of variability that may affect the HCF resistance of the periodic cellular structures are mainly of three types:

- Surface roughness, which involves a very large amount of very local defects with a typical depth of 10 μm (Fig. 4(b)).
- Deviations from the nominal CAD geometry due to the instability of the molten pool, which sporadically causes a severe local reduction (typically 200 μm) of the strut diameter or wall thickness (from a typical 500 μm value), as well as a less significant (typically 50 μm) but more widespread deviation depending on the building angle (Fig. 7 and Table 5).
- Local microstructure, which may reduce or increase the consequences of the above-mentioned defects (Fig. 9).

The combined use of the statistics of extremes and the Crossland HCF criterion has proved to be an appropriate way to numerically assess the effect of the surface roughness on the HCF strength of bulk HIPed Ti-6Al-4V specimens [26]. In periodic cellular structures, it is also necessary to take into account the deviations from the nominal CAD geometry in order to properly assess the HCF resistance of the whole structure. Characterizing the deviation and its variability is very challenging as it requires a large amount of experimental data. In this paper, only the very first step is carried out: identify promising EC geometries regarding HCF strength under multiaxial loadings. The flow-chart of the numerical strategy developed in this work is illustrated in Fig. 11. The aim of such a strategy is twofold. First, a set of six static analyses is conducted in order to retrieve the homogenised macroscopic elastic behaviour of each EC. Second, a fatigue analysis under periodic boundary conditions is conducted on each EC, thus considering the EC is embedded in an infinite medium. This is a strong assumption, as mechanical fields are clearly altered by the presence of a surface, even several cells away, but this issue will be addressed in future work.

The fatigue strength is post-processed using the stress fields at each node. First, both the maximum hydrostatic stress and the alternating octahedral shear stress over a cycle are calculated in order to compute a Crossland's Fatigue Indicator Parameter (FIP) at each node of the EC mesh. Second, only the top 5% of the FIP's values are considered, and the median value of this population is retained as the fatigue strength.

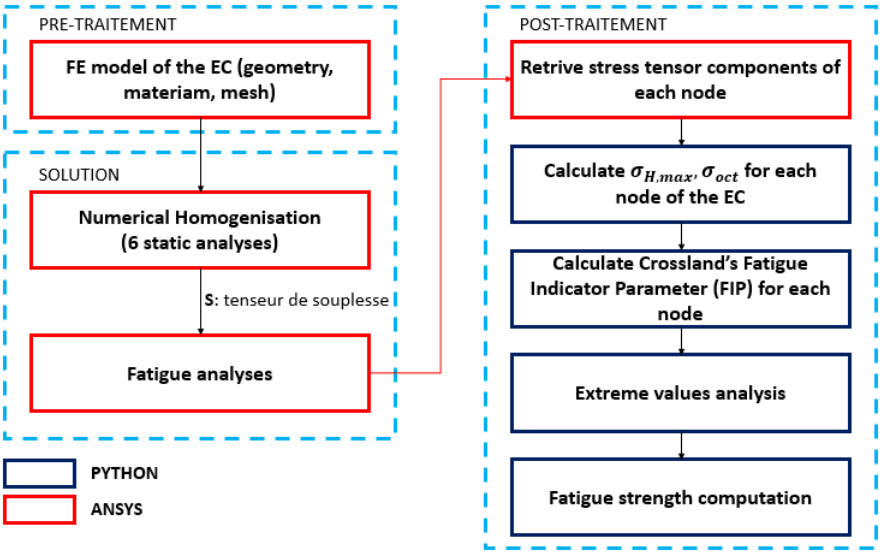

Figure 11: Numerical procedure.

The FE model of the EC and the periodic boundary conditions (PBCs) used for numerical homogenisation and fatigue analysis are described in Section 4.1, whilst the Fatigue Indicator Parameter and the Extreme Values analysis are detailed in the next two subsections.

4.1. Finite Element model of the Elementary Cell

The FE models of the ECs have been created within the commercial FE code ANSYS®. These models were generated through an *ad-hoc* script in which the mesh is properly related to the relevant geometric parameters of the EC. Each EC was modelled by means of 20-nodes solid elements (SOLID186), with three DOFs per node. A FE model made of solid elements is needed to provide both a realistic representation of the EC geometry and an accurate assessment of the 3D stress fields inside the EC.

4.1.1. Boundary conditions for the homogenisation analysis

At the mesoscopic scale, the EC of the periodic cellular structure can be interpreted, from a mechanical point of view, as an heterogeneous medium composed of two phases, i.e. the bulk material and the void. Conversely, at the macroscopic scale it can be modelled as an equivalent homogeneous anisotropic continuum whose mechanical response is described by a set of *effective* (or equivalent) material properties.

The set of effective elastic properties of the EC can be determined through a suitable numerical homogenisation technique. Indeed, although the bulk material constituting the EC is isotropic, its macroscopic behaviour (i.e. after homogenisation) can be anisotropic because the effective elastic properties depend upon the EC topology which strongly affects the stiffness tensor of the homogeneous material at the upper scale by introducing some preferential orientations (according to the symmetries of the EC).

The effective properties of the EC are determined using the strain energy homogenisation technique of periodic media [15]. This technique makes use of the repetitive unit of the periodic structure to evaluate the resulting elastic behaviour at the macroscopic scale. The basic feature of the strain energy homogenisation technique is the assumption that the EC of the periodic structure and the corresponding volume of the homogeneous solid undergo the same deformation, having, hence, the same total strain energy. This homogenisation scheme has proven to be an efficient numerical procedure able to determine

the equivalent properties of different heterogeneous materials characterised by complex EC topologies. The strain energy homogenisation technique of periodic media based on volume averaged stresses has already been utilised in other works, see [16, 17, 27–36] for further details.

In order to evaluate the elastic response of the EC at the macroscopic scale, two main hypotheses have been considered:

- linear, elastic behaviour for the bulk material of the EC;
- the buckling of the cell struts/walls is disregarded.

In order to compute the EC effective elastic properties (stiffness tensor $\mathbf{C}$), suitable boundary conditions (BCs) must be considered and an appropriate post-processing procedure must be carried out on the complex stress field resulting from the application of these BCs.

The EC is submitted to an average strain field ε^0_{ij}, with $i,j = 1,2,3$ (tensor notation). The six independent components of the average strain tensor are applied by considering a set of periodic boundary conditions (PBCs) on the EC [15]:

$$\begin{cases} u_i(a_1,x_2,x_3) - u_i(-a_1,x_2,x_3) = 2a_1\varepsilon^0_{i1}, & (-a_2 \le x_2 \le a_2,\ -a_3 \le x_3 \le a_3), \\ u_i(x_1,a_2,x_3) - u_i(x_1,-a_2,x_3) = 2a_2\varepsilon^0_{i2}, & (-a_1 \le x_1 \le a_1,\ -a_3 \le x_3 \le a_3), \\ u_i(x_1,x_2,a_3) - u_i(x_1,x_2,-a_3) = 2a_3\varepsilon^0_{i3}, & (-a_1 \le x_1 \le a_1,\ -a_2 \le x_2 \le a_2), \end{cases} \tag{4}$$

where $i = 1,2,3$.

These PBCs result in a complex stress field inside the EC. The applied average strains always meet the following condition:

$$\overline{\varepsilon}_{ij} = \frac{1}{V_{\mathrm{EC}}} \int_{V_{\mathrm{EFF}}} \varepsilon_{ij}\, dV = \varepsilon^0_{ij},\ \ i,j = 1,2,3. \tag{5}$$

In the previous equation V_{EFF} is the actual volume of the EC which is different from the overall volume of the EC, i.e. V_{EC}, due to the presence of void. The constitutive law for the equivalent homogeneous material (at the macroscopic scale) can be obtained as (Voigt's notation):

$$\overline{\sigma}_\alpha = C_{\alpha\beta}\overline{\varepsilon}_\beta, \quad \alpha,\ \beta = 1,..6. \tag{6}$$

In the previous equation Einstein's summation convention on repeated indexes is tacitly assumed. The components of the stiffness tensor $C_{\alpha\beta}$ are then determined by solving six static analyses on the EC and by imposing the previous PBCs, where only one component at time of the strain ε^0_β is different from zero for each one of the six problems.

For each static analysis, the volume-averaged value of each component of the stress field $\overline{\sigma}_\alpha$ can be easily computed and the stiffness matrix of the equivalent homogeneous material can be calculated column-wise as:

$$C_{\alpha\beta} = \frac{1}{V_{\mathrm{EC}}\varepsilon^0_\beta} \int_{V_{\mathrm{EFF}}} \sigma_\alpha(x_1,x_2,x_3)\, dV,\ \ \varepsilon^0_\gamma = 0,\ \ \gamma = 1,\cdots,6,\ \ \gamma \neq \beta. \tag{7}$$

The engineering moduli of the equivalent homogeneous anisotropic continuum can be calculated starting from the components of the compliance tensor $\mathbf{S}$ as:

$$\mathbf{S} = \mathbf{C}^{-1}. \tag{8}$$

A convergence study in terms of the average element size (not reported here for the sake of brevity) has been conducted in order to verify its influence on the effective elastic properties of the different EC topologies. The mesh size has been chosen equal to 0.05 mm for a cell size equal to 3 mm.

4.1.2. Boundary and loading conditions for the fatigue analysis

The fatigue analysis considered in this study assumes that, in the high-cycle fatigue regime and using the extreme values theory, an elastic constitutive law is sufficient for assessing stress fields in the EC.

The fatigue analysis is carried out on the EC at the mesoscopic scale by applying macroscopic cyclic loads $\overline{\boldsymbol{\sigma}}(t)$ through an equivalent strain field at the mesoscopic scale of the EC.

The bearable shear stress amplitude and normal stress amplitude of the EC has been assessed by considering five loading conditions $\text{Ł}_{\mathbf{k}}$, $k = 1, ..., 5$ at the macroscopic scale. Except for Table 9, where $R_\sigma = 0.1$ to allow comparison with experimental results, all calculations were performed for $R_\sigma = -1$. The equivalent strain field to be applied to the EC at the mesoscopic scale (which corresponds to a specific cyclic stress state $\overline{\boldsymbol{\sigma}}(t)$ at the upper scale) has been introduced by means of the PBCs of Eq. (4) where the average strain tensor $\varepsilon^{\mathbf{0}}_{\mathbf{k}}$, for each load case $k = 1, ..., 5$, have been determined as:

$$
\begin{cases}
\boldsymbol{\varepsilon}^{\mathbf{0}}_{\mathbf{1}} = \mathbf{S} : \begin{bmatrix} 0 & 0 & 0 \\ 0 & \overline{\sigma}(t) & 0 \\ 0 & 0 & 0 \end{bmatrix}, & (L_1) \\
\boldsymbol{\varepsilon}^{\mathbf{0}}_{\mathbf{2}} = \mathbf{S} : \begin{bmatrix} 0 & \overline{\tau}(t) & 0 \\ \overline{\tau}(t) & 0 & 0 \\ 0 & 0 & 0 \end{bmatrix}, & (L_2) \\
\boldsymbol{\varepsilon}^{\mathbf{0}}_{\mathbf{3}} = \mathbf{S} : \begin{bmatrix} 0 & \overline{\tau}(t) & 0 \\ \overline{\tau}(t) & \overline{\sigma}(t) & 0 \\ 0 & 0 & 0 \end{bmatrix}; \quad \overline{\tau}_a = \overline{\sigma}_a, & (L_3) \\
\boldsymbol{\varepsilon}^{\mathbf{0}}_{\mathbf{4}} = \mathbf{S} : \begin{bmatrix} 0 & \overline{\tau}(t) & 0 \\ \overline{\tau}(t) & \overline{\sigma}(t) & 0 \\ 0 & 0 & 0 \end{bmatrix}; \quad \overline{\tau}_a = \frac{\overline{\sigma}_a}{3}, & (L_4) \\
\boldsymbol{\varepsilon}^{\mathbf{0}}_{\mathbf{5}} = \mathbf{S} : \begin{bmatrix} 0 & \overline{\tau}(t) & 0 \\ \overline{\tau}(t) & \overline{\sigma}(t) & 0 \\ 0 & 0 & 0 \end{bmatrix}; \quad \overline{\tau}_a = 3 \times \overline{\sigma}_a. & (L_5)
\end{cases}
\tag{9}
$$

In Eq. (9), $\mathbf{S}$ is the compliance tensor determined after numerical homogenisation according to Eq. (8). The results (in terms of displacement, strain and stress fields), provided by the fatigue analysis conducted on the mesoscopic FE model of the EC, have been post-processed by means of a suitable numerical procedure wherein the ANSYS® FE model has been interfaced with in-house routines (programmed in PYTHON environment).

Even for the fatigue analysis, it was observed that a mesh size of 0.05 mm for a cell size equal to 3 mm is sufficient to properly evaluate the EC fatigue strength, except in presence of fillet radii (Fig. 13) or when rough surfaces reconstructed from the μCT are considered (Fig. 16(b)). According to the convergence study, the mesh size in these cases was decreased to 0.03 mm and 0.007 mm, respectively.

4.2. Multiaxial high-cycle fatigue criterion

Fatigue criteria available in the literature can be classified into three families: (i) phenomenological criteria based on tensor invariants [37, 38], (ii) criteria based on the definition of the critical plane in the space of stress / strain tensor components [39–41] or (iii) energy based HCF criteria [42–45].

The vast majority makes use of variables depending on the stress tensor $\boldsymbol{\sigma}(\mathbf{x}, t)$ and/or strain tensor $\boldsymbol{\varepsilon}(\mathbf{x}, t)$ and possibly additional variables noted here V_i. The multiaxial high-cycle fatigue criterion used in this work has the form

$$f(\boldsymbol{\sigma}(\mathbf{x}, t), \boldsymbol{\varepsilon}(\mathbf{x}, t), V_i) \leq 0. \tag{10}$$

A fatigue criterion assumes that in the vicinity of the considered point the material is in a stabilised state of stresses and deformations in order to be able to apply a criterion by considering only variables calculated on a single loading cycle. This condition of stabilisation of the behaviour is indispensable and certainly verified here, as an elastic constitutive law is used.

Generally speaking, Eq. (10) defines a no-onset (limit state) condition for the fatigue cracks under cyclic loads for a high number of cycles (typically higher than 10^6 or 10^7) and a fixed survival probability P_s.

The criterion considered in this study belongs to the first family: the Crossland's criterion which makes use of a linear combination of the maximum hydrostatic stress $\sigma_{H,\max}$ over a cycle and of the amplitude of the second invariant of the deviatoric part of the stress tensor $\sqrt{J_{2a}}$, i.e.

$$\sqrt{J_{2a}} + \alpha\sigma_{H,\max} < \beta, \tag{11}$$

where α and β are two parameters depending upon material and process, which are measured for a given number of cycles. In this study, these parameters were taken from the work of Vayssette *et al.* [46] for Ti-6Al-4V specimens manufactured by Selective laser melting (SLM), then subject to Hot Isostatic Pressing (HIP), with two different surface conditions: as-built or machined. Values are $\alpha = 0.908$ and $\beta = 195.8$ MPa for as-buit surfaces, $\alpha = 0.86$ and $\beta = 442.7$ MPa for machined surfaces, both at 2x10^6 cycles.

J_{2a} is the radius of the smallest hypersphere embedding the loading path in the space of the deviatoric part of the stress tensor components, computed over a loading cycle according to the following expression:

$$\sqrt{J_{2a}} = \max_{t \in T} \sqrt{(\boldsymbol{\sigma}_d - \boldsymbol{\sigma}_{dm}) : (\boldsymbol{\sigma}_d - \boldsymbol{\sigma}_{dm})}. \tag{12}$$

In Eq. (12), $\boldsymbol{\sigma}_d$ and $\boldsymbol{\sigma}_{dm}$ are the deviatoric part and the average deviatoric part (denoting the center of the hypersphere obtained by the equation) of the stress tensor, respectively. t and T are the time and the loading period, respectively. $\boldsymbol{\sigma}_{dm}$ is defined as:

$$\boldsymbol{\sigma}_{dm} = \min_{\boldsymbol{\sigma}'_d} (\max_{t \in T} \sqrt{(\boldsymbol{\sigma}_d - \boldsymbol{\sigma}'_d) : (\boldsymbol{\sigma}_d - \boldsymbol{\sigma}'_d)}). \tag{13}$$

In Eq. (11), $\sigma_{H\max}$ is the maximum hydrostatic stress over a cycle, which can be written

as:

$$\sigma_{H,\max} = \frac{1}{3}\max_{t\in T}\sum_{k=1}^{3}\sigma_{kk}, \tag{14}$$

where σ_{kk} $(k = 1, 2, 3)$ are the diagonal elements of the stress tensor.

In this study, the Crossland's criterion is considered in the case of multiaxial *proportional loads*, a particular loading condition wherein both the direction and the ratio R_σ of principal stresses are constant. For proportional loads the second invariant of the stress tensor reads:

$$J_{2a} = \frac{1}{6}[(\sigma_{\mathrm{I}a} - \sigma_{\mathrm{II}a})^2 + (\sigma_{\mathrm{I}a} - \sigma_{\mathrm{III}a})^2 + (\sigma_{\mathrm{II}a} - \sigma_{\mathrm{III}a})^2], \tag{15}$$

4.3. Extreme Values Theory

The stress and strain fields in the ECs (at the mesoscopic scale) are strongly heterogeneous. In addition, their gradients are substantial, due to small dimensions. In such cases, using only local (nodal) values to evaluate the fatigue strength usually is inadequate. The EVT framework is chosen to overcome this issue. The proposed approach is based on the extreme value distribution of a fatigue indicator parameter (FIP) related to the Crossland's criterion:

$$FIP = \sqrt{J_{2a}} + \alpha\sigma_{H,\max}. \tag{16}$$

Let Ω_n be the set gathering the FIPs such that $\Omega_n = \{\mathrm{FIP}_1, \mathrm{FIP}_2, ..., \mathrm{FIP}_n\}$. Let $M_n = \max\{\mathrm{FIP}_1, \mathrm{FIP}_2, ..., \mathrm{FIP}_n\}$ be the maximum value. The probability that the latter is lower than σ^* is the probability that none of the n values is greater than σ^*, i.e.

$$P(\Omega_n < \sigma^*) = P(M_n < \sigma^*). \tag{17}$$

According to the Fisher-Tippett-Gnedenko theorem [47], if a sequence of pairs of real numbers (a_n, b_n) exists such that each $a_n < 0$ and $\lim_{n\to+\infty} P\left(\frac{M_n - b_n}{a_n} \leq \sigma\right) = G(\sigma)$, where G is a non-degenerate distribution function, then G belongs to either the Gumbel, the Fréchet or the Weibull family. Jenkinson [48] combined the three limit distributions in a single parametric form called Generalized Extreme Value (GEV) distribution depending on a single parameter ξ:

$$G(x) = \begin{cases} \exp(-(1+\xi x)^{-\frac{1}{\xi}}) \text{ if } \xi \neq 0, \forall x : 1 + \xi x > 0, \\ \exp(-\exp(-x)) \text{ if } \xi = 0. \end{cases} \tag{18}$$

The parameter ξ is called extreme index. Its sign denotes the type of asymptotic distribution: Weibull ($\xi < 0$), Gumbel ($\xi = 0$) or Fréchet ($\xi > 0$). The variable $\frac{M_n - b_n}{a_n}$ is called normalised maximum of the random variable σ. The parameters a_n and b_n are called shape factors of the distribution.

Applying this method requires identifying the size of the extreme values population that ensures statistical representativeness. In the present study, due to a lack of experimental data and for comparative purpose, the size of the extreme values population is a percentage of nodes (then of volume), which is the same for all EC geometries. The larger the population, the lower the median value of the cumulative probability distribution, which

is retained as the fatigue strength. The variation of the median value with the population size shows a typical shape with three sections: (i) a fast decrease as FIP values in the vicinity of the most critical nodes are included, (ii) a slowing decrease as new FIP values further from the critical nodes are considered, (iii) an asymptote as remaining FIP values are outside of the stress gradients. Depending on the EC, the decrease speed is slightly different, but we considered a unique value of 5% of the nodes to define the extreme values population, as it allows to be in the second section for all the ECs. One should note that the median of the top 5% FIP values is also the maximum of the FIP values once the top 2.5% are discarded. The sensitivity to the size of the extreme values population in the 3% - 7% range has been added in Appendix for octet and thin-walled gyroid ECs.

Finally, the fatigue strength $\overline{\sigma}_D$ (for a unit safety factor, i.e. SF= 1, then when the FIP value is equal to the Crossland parameter β) can be expressed as

$$\overline{\sigma}_D = \frac{\overline{\sigma}_0 \times \beta}{\sigma^*} \tag{19}$$

where $\overline{\sigma}_0$ is the amplitude of the arbitrary initial applied load, σ^* the FIP value obtained for $\overline{\sigma}_0$.

5. Numerical results

5.1. Fatigue strength of the different EC topologies

A first numerical campaign of analyses has been carried out in order to compare the fatigue strength of the different EC topologies which are summarised in Tables 6-7 for a relative density equal to 10%, i.e. $\overline{\rho} = 0.1$. As a consequence of the definition of the macroscopic stress (explained in section 3.6), the fatigue strength values are reduced due to the $\overline{\rho} = 0.1$ relative density. As an example, an EC made of vertical struts loaded in the same direction would exhibit a fatigue strength that is one tenth that of the bulk material (with rough surface). As an other example, the CC EC (Fig. 1) is made of struts in the three directions, so its fatigue strength under tension for a given density might be as low as one third that of the first example, as almost two thirds of the material are not loaded. This reduction is observed for all ECs in Tables 6 and 7, as no direction is favoured and $\overline{\rho} = 0.1$. For the first class (Table 6), results show that BCC EC has the lowest fatigue strength in tension but the highest in shearing. Conversely, CC EC has the highest fatigue strength in tension and the lowest in shearing. These results are in agreement with the topologies of these two ECs, whose struts are essentially oriented along axes (CC) or diagonals (BCC) [18]. Also, the combination of different ECs may offer a better fatigue strength under combined tension and shear loadings (e.g. the CBCC EC which is a combination of CC and BCC).

EC	Tension (L_1) [MPa]	Torsion or pure shear (L_2) [MPa]	Combined tension and torsion with $\overline{\tau}_a = \overline{\sigma}_a$ (L_3) [MPa]	Combined tension and torsion with $\overline{\tau}_a = \frac{\overline{\sigma}_a}{3}$ (L_4) [MPa]	Combined tension and torsion with $\overline{\tau}_a = 3 \times \overline{\sigma}_a$ (L_5) [MPa]
ACC	10.3	7.2	7.9	10.3	7.2
BCC	2	10.2	2.8	2.1	5.1
BFCC	8.2	9.9	7.6	7.8	8.7
CBCC	8.1	8.5	8.9	8.1	8.6
CBFCC	7.6	9	8.6	8	8.7
CC	18.2	1.7	2.3	4.8	1.8
CIC	7.3	1.7	2.4	5	1.8
CFCC	11.3	7.3	7.9	10.6	7.2
Diamond	3.1	3.4	3.2	3.2	3.3
FCC	9.7	7.4	7.9	9	7.6
FCC2+	8.8	7.2	7.4	8.2	7.2
Hexahedral	17.4	1.5	2	4.3	1.5
Octahedral	6.8	7.3	6.6	6.9	6.9
Octet	12	10	8.4	10	8.6
Rhombic	2.5	2.8	2.6	2.5	2.7
Truncated-cube	10.7	5.8	7	9.6	6
Truncated-cubo	5.1	2.7	3.2	4.3	2.8
Truncated-cubo2+	5.9	3.2	4	5.4	3.4

Table 6: Assessed fatigue strength of the different strut-based EC topologies under the 5 loading cases of Eq. (9), for $\overline{\rho} = 0.1$ and $L = 3mm$.

As it clearly appears when looking at the EC topologies composed of struts, the stress concentration occurs at the intersection of struts withstanding the applied load. These localised stress concentration zones strongly affect the fatigue strength. Conversely, TPMS-based ECs show a fatigue strength higher than that characterising those made of struts, as shown in Table 7. This is due to the fact that these structures are free of connecting nodes or sharp edges.

It is noteworthy that the highly complex thin-walled TPMS are characterised by fatigue strength values that are higher than those typical of strut-based and skeletal-based cellular structures, showing, thus, a higher structural efficiency, see Table 7. Among the investigated ECs, the highest fatigue strength occurs for Gyroid configuration.

Skeletal EC	Tension (L_1) [MPa]	Torsion or pure shear (L_2) [MPa]	Combined tension and torsion with $\overline{\tau}_a = \overline{\sigma}_a$ (L_3) [MPa]	Combined tension and torsion with $\overline{\tau}_a = \frac{\overline{\sigma}_a}{3}$ (L_4) [MPa]	Combined tension and torsion with $\overline{\tau}_a = 3 \times \overline{\sigma}_a$ (L_5) [MPa]
BTC	16.5	2.4	3	4.9	2.5
Gyroid	7.5	9.9	8.6	7.7	9.7
iBCC	12.6	4.1	5.3	9.7	4.3
IWP	3.8	10.9	4.6	3.9	7.3
OrthoCircle	7.6	3.9	4.3	5	4
Schwarz	7.6	4.4	5.2	6.4	4.5
Thin-walled EC	Tension (L_1) [MPa]	Torsion or pure shear (L_2) [MPa]	Combined tension and torsion with $\overline{\tau}_a = \overline{\sigma}_a$ (L_3) [MPa]	Combined tension and torsion with $\overline{\tau}_a = \frac{\overline{\sigma}_a}{3}$ (L_4) [MPa]	Combined tension and torsion with $\overline{\tau}_a = 3 \times \overline{\sigma}_a$ (L_5) [MPa]
Batwing	9.6	7.3	8.3	9.3	7.5
BTC	7.7	4	5.3	7.2	4.2
F-RD	9.9	7.2	8.5	9.5	7.5
Gyroid	16.3	11.5	12.3	14.6	11.4
IWP	14.7	9	10.3	13.1	9.2
Manta	12.9	11.5	11.8	12.6	11.4
Neovius	13.9	4.4	6.1	10.6	4.7
Schone-I6	7.9	6.9	7.2	7.6	7.4
Schwarz	8.3	6.4	7.1	8.2	6.5

Table 7: Assessed fatigue strength of the different skeletal TPMS and thin-walled TPMS EC topologies under the 5 loading cases of Eq. (9), for $\overline{\rho} = 0.1$ and $L = 3mm$.

5.2. Influence of the relative density on fatigue strength

A second numerical campaign of analyses has been carried out in order to investigate the influence of the EC relative density on its fatigue strength. For the sake of brevity, only the results of two types of ECs, namely Octet and thin-walled Gyroid, are presented and discussed. For each case the relative density varies between 0.1 and 0.4 which are classical values taken from literature. As expected, the higher the relative density, the higher the fatigue strength. As illustrated in Fig. 12(b) and 12(d), after normalising the stress amplitudes with respect to the relative density, curves are more or less represented by a single power law for each type of EC.

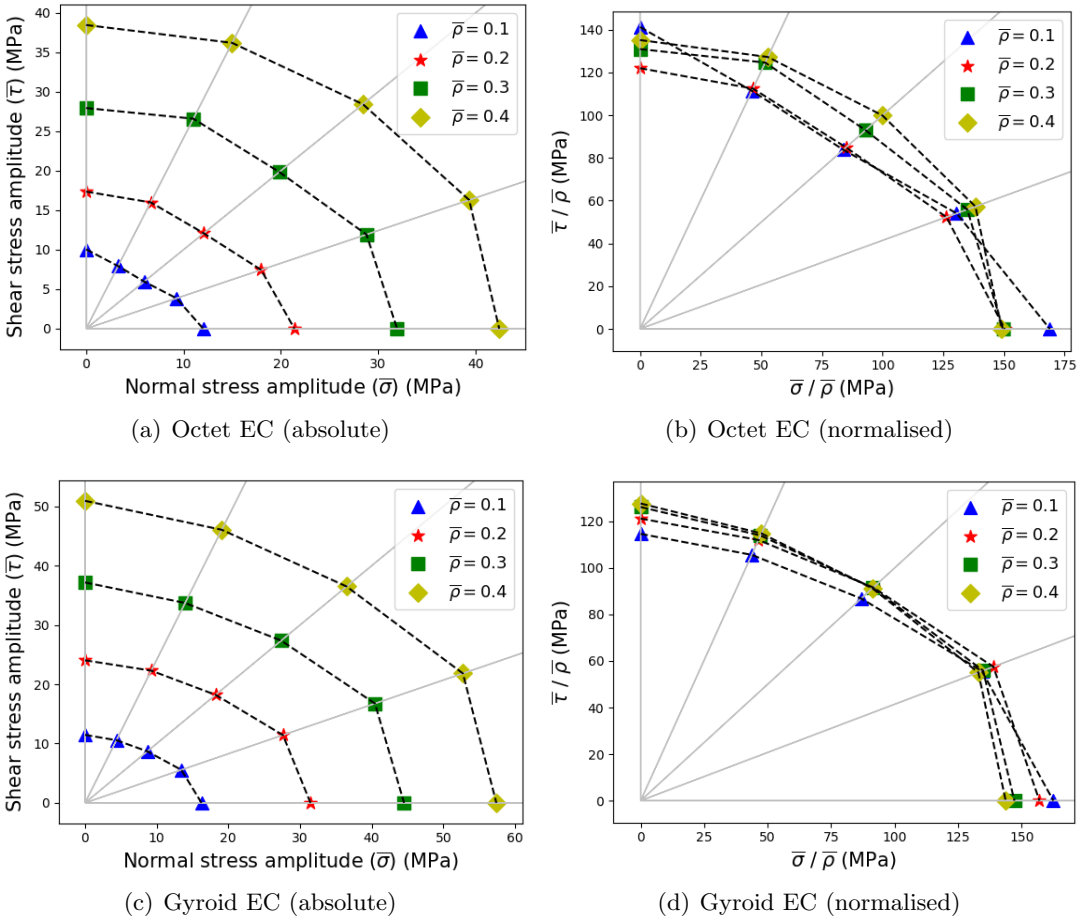

(a) Octet EC (absolute)

(b) Octet EC (normalised)

(c) Gyroid EC (absolute)

(d) Gyroid EC (normalised)

Figure 12: Simulated bearable shear stress amplitude versus the normal stress amplitude for different fully reversed loadings (from pure shear to pure tension with three combined tension and torsion loadings), for the octet EC and the thin-walled Gyroid EC. Stress amplitudes are either absolute or normalised with respect to the relative density ranging from 0.1 to 0.4.

5.3. Influence of the introduction of spherical nodes or fillet radius on fatigue strength

Refai *et al.* [18] showed that the presence of local geometrical features like spherical nodes and/or fillet radius to join the EC branches strongly affects the stress field at the mesoscopic scale and, consequently, the equivalent elastic behaviour at the macroscopic scale. By following the same approach, the effect of these features on the fatigue strength of EC can be investigated: for sake of brevity only the results of the Octet EC for $d_{CAD} = 0.52mm$ are discussed in the following. An illustration of the Octet configuration with spherical nodes as well as fillet radius joining the elementary struts is given in Fig. 13 for different values of the sphere diameter Ω and the fillet radius R. In this picture, the sphere diameter and the fillet radius are expressed as a function of the strut diameter, i.e. $\Omega = \delta d_{CAD}$ and $R = \gamma d_{CAD}$.

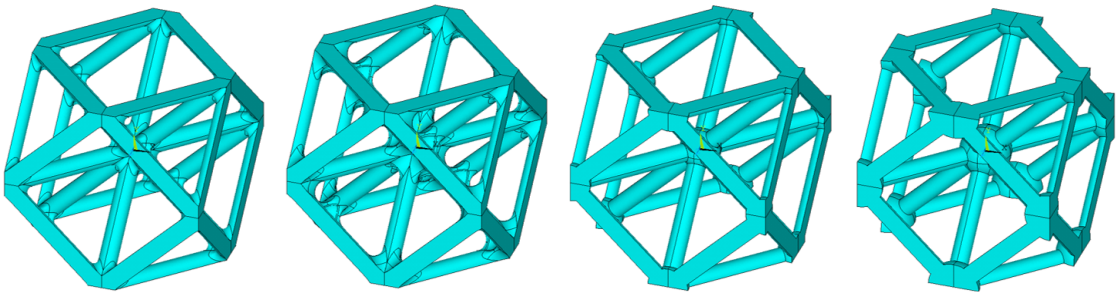

(a) (b) (c) (d)

Figure 13: Octet EC with a: fillet radius $R = \frac{1}{3}d_{CAD}$, b: fillet radius $R = \frac{2}{3}d_{CAD}$, c: spherical nodes of diameter $\Omega = 2.4 \times d_{CAD}$ and d: spherical nodes of diameter $\Omega = 2.8 \times d_{CAD}$.

Fig. 14(a) shows the trend of the fatigue strength of the Octet EC vs. the γ coefficient, for $d_{CAD} = 0.52mm$ and for a cell size L equal to 3 mm, corresponding to $\overline{\rho} = 0.3$. Fig. 14(b), illustrates the normalised fatigue strength curve. The latter is very important because when the fillet radius varies the EC relative density changes too.

As it can be easily inferred from Fig. 14(a), the presence of a fillet radius joining concurrent struts allows for increasing the fatigue strength of the lattice. Moreover, the greater the fillet radius the greater the relative density. As illustrated in Fig. 14(b), for standard values of the fillet radius (i.e. values that can properly be obtained by means of SLM process) the fatigue strength always grows almost as fast as the relative density. Accordingly, a lattice characterised by fillet radius is always a lightweight structure.

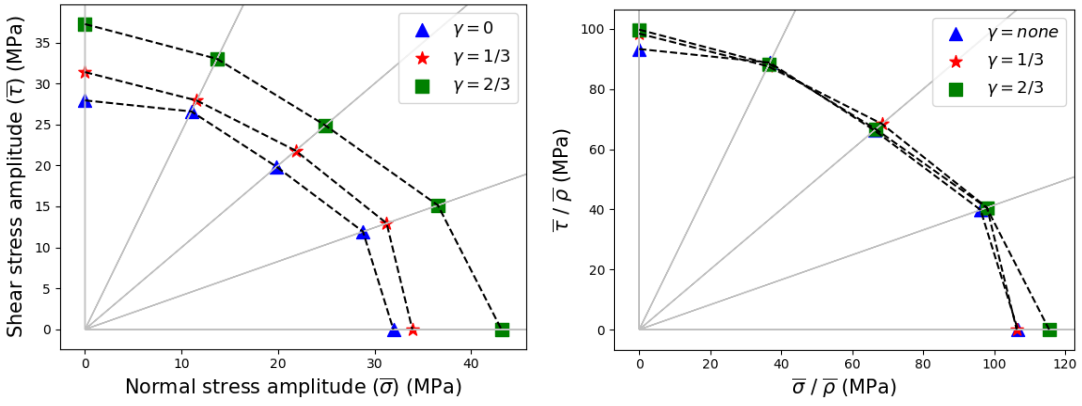

(a) Absolute (b) Normalised

Figure 14: Simulated bearable shear stress amplitude versus the normal stress amplitude for different fully reversed loadings (from pure shear to pure tension with three combined tension and torsion loadings), for the octet EC with $d_{CAD} = 0.52mm$ and three values of the fillet radius. Stress amplitudes are either absolute (a) or normalised with respect to the relative density (b).

Fig. 15(a) shows the trend of the fatigue strength vs. the δ coefficient, for $d_{CAD} = 0.52mm$ and for a cell size L equal to 3 mm, corresponding to $\overline{\rho} = 0.3$. Fig. 15(b) illustrates the normalised fatigue strength curves.

An analysis of Fig. 15(a) suggests that the presence of spherical nodes between struts leads to a slight overall enhancement of the fatigue strength. But this increment is lower than that obtained for the solution characterised by fillet radius. Besides, the greater the sphere diameter the greater the relative density. As illustrated in Fig. 15(b), the relative

density grows faster than the fatigue strength in this case: accordingly, the strength-to-weight ratio of the structure decreases. Conversely, when studying the mechanical behaviour of the octet EC as shown in [18], the presence of a spherical node joining the struts allows for increasing the macroscopic elastic properties in a monotonic non-decreasing fashion.

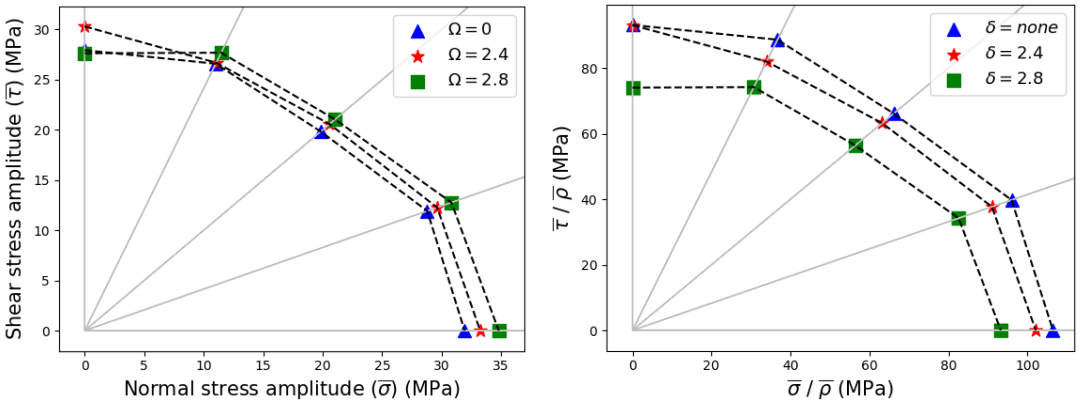

(a) Absolute (b) Normalised

Figure 15: Simulated bearable shear stress amplitude versus the normal stress amplitude for different fully reversed loadings (from pure shear to pure tension with three combined tension and torsion loadings), for the octet EC with $d_{CAD} = 0.52mm$ and three values of the sphere diameter. Stress amplitudes are either absolute (a) or normalised with respect to the relative density (b).

5.4. Influence of the surface roughness effect on fatigue strength

The following methodologies have been conducted on the Octet EC to take into account the notch effect of the surface roughness on the fatigue strength:

- Method1: Rough surfaces are taken into account by using the $\alpha = 0.908$ and $\beta = 195.8$ MPa parameters determined at 2x10^6 cycles for as-built surfaces characterized by $R_a = 19\mu m$ and $R_v = 74\mu m$ [26]. CAD geometry is used. Results are plot using squares on Fig. 17.

- Method2: Rough surfaces are obtained from CAD geometry through a small (random) perturbation of the location of nodes belonging to the EC external surfaces (the perturbation has been introduced along the local normal at each point of the surface), see Fig. 16(a). The values of strut diameter $d = \overline{d}_{mean}$ and strut surface roughness R_a are listed in Table 8. $\alpha = 0.86$ and $\beta = 442.7$ MPa parameters determined at 2x10^6 cycles for machined surfaces are used. Results are plot using diamonds on Fig. 17.

θ	0°	35.26°	45°
$\frac{d}{d_{CAD}}$	99 %	95.6%	97.1%
$R_a(\mu m)$	43.75	37.5	29.25

Table 8: Values of strut diameter d and strut surface roughness R_a with respect to its building angle θ. $d_{CAD} = 0.55mm$ and $L = 4mm$

- Method3: Rough surfaces are reconstructed from the μCT imaging, see Fig. 16(b).

α and β parameters for machined surfaces are used. Results are plot using stars on Fig. 17.

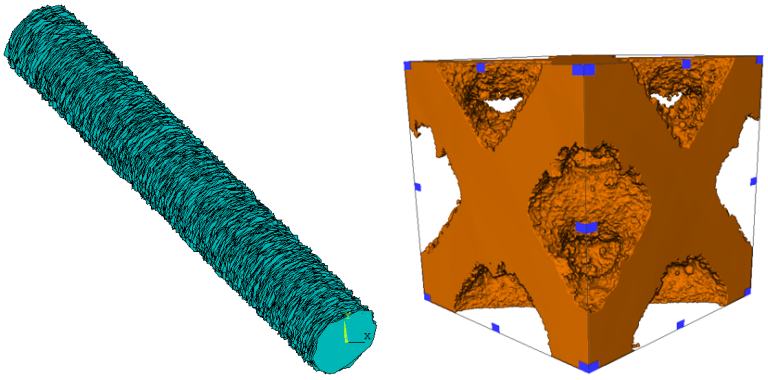

(a) (b)

Figure 16: Images of (a) generated strut with rough surface (b) μCT reconstructed EC.

These methodologies are compared with the one used in the previous subsections (CAD geometry, α and β parameters for machined surfaces), whose results are plot using triangles on Fig. 17. As expected, surface roughness has a very strong effect on the fatigue strength. The differences between the three methodologies are less pronounced. Lower assessed fatigue strengths are obtained using μCT geometry (Method3). Larger assessed fatigue strengths are obtained using CAD (smooth) geometry and Crossland parameters for as-built (rough) surfaces (Method1).

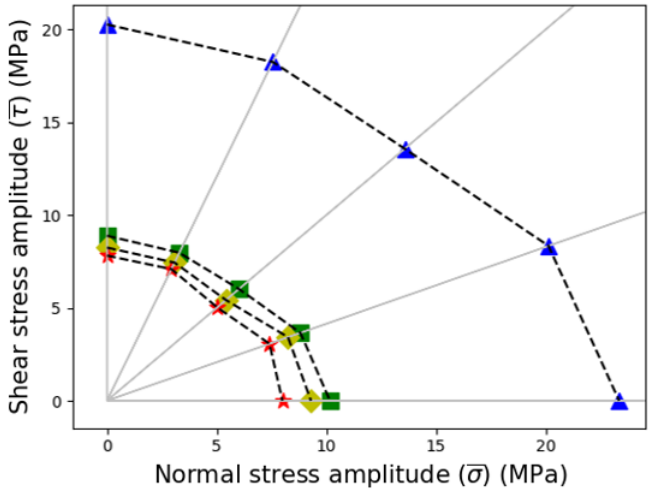

Figure 17: Simulated bearable shear stress amplitude versus the normal stress amplitude for different fully reversed loadings (from pure shear to pure tension with three combined tension and torsion loadings), for the octet EC with a size $L = 4mm$ and a relative density $\overline{\rho} = 0.2$: (triangles) without surface roughness, (squares) using Crossland parameters on rough surfaces, (diamonds) using rough CAD geometry, (stars) using μCT geometry.

5.5. Comparison with experimental results

The experimental fatigue strengths determined in tension by the staircase method at 10^6 cycles are listed in Table 9 and compared with numerical results. The chosen fatigue criterion (median of EV of FIP) combined to the best geometric description, i.e. the

μCT reconstructed volume (Method3), or to a simulated geometric description (Method2) provide accurate assessment of the Octet fatigue strength in tension.

Still, Method1 is an easy and fast way to obtain a first order estimation of the fatigue strength of cellular structures. Results obtained by this method for Gyroid EC are even closer to the experimental data.

EC	Octet	Gyroid
$\overline{\sigma}_{D,exp}$ (MPa)	12.3	19.7
$\overline{\sigma}_{D,num}$ (MPa) [Method1]	14.3	19.2
$\overline{\sigma}_{D,num}$ (MPa) [Method2]	13.1	-
$\overline{\sigma}_{D,num}$ (MPa) [Method3]	11.3	-

Table 9: Experimental and assessed fatigue strengths of Octet and Thin-walled gyroid structures for $R_\sigma = 0.1$.

6. Conclusions and prospects

A methodology based on both the statistics of extremes and the Crossland HCF criterion has been proposed in order to investigate the influence of the Elementary Cell topology on the fatigue resistance of several classes of cellular structures under proportional multiaxial loading. Thin-walled TPMS show the better fatigue strength when compared to lattice and skeletal TPMS, and therefore a higher structural efficiency. Among lattices and thin-walled TPMS respectively, the octet and gyroid are showing the better overall fatigue resistance, under tension, torsion or combined proportional loadings, and this fatigue resistance is proportional to the relative density in the 0.1 to 0.4 range.

Single struts with various diameters, lengths and building angles were produced using SLM technology with standard process parameters. Printing quality was assessed using OM, SEM and μCT techniques. The major source of discrepancy with the CAD geometry proved to be the surface roughness, especially on the lower face of the most inclined struts, leading to significant shape and size differences between the nominal cross-sections of the struts and the manufactured ones.

Finally, three methods to numerically assess the effect of the surface roughness on the HCF strength were compared. Their predictions are close, and in accordance with experimental results in tension on octet and thin-walled gyroid structures.

These methods are taking into account the local surface roughness, but not the larger deviations from the nominal CAD geometry. In order to properly assess the HCF resistance of a whole periodic cellular structure, it is still necessary (i) to characterize experimentally the deviation and its variability, on the two promising EC geometries identified in this study, (ii) to assess its effect on the HCF strength using the proposed methodology, (iii) and to estimate the border effects related to the presence of a free border or a skin.

Appendix A.

Octet

% of EV	Tension (L_1) [MPa]	Torsion or pure shear (L_2) [MPa]	Combined tension and torsion with $\overline{\tau}_a = \overline{\sigma}_a$ (L_3) [MPa]	Combined tension and torsion with $\overline{\tau}_a = \frac{\overline{\sigma}_a}{3}$ (L_4) [MPa]	Combined tension and torsion with $\overline{\tau}_a = 3 \times \overline{\sigma}_a$ (L_5) [MPa]
3%	-13.34%	-15.15%	-3.61%	-6.06%	-4.65%
7%	4.85%	3.03%	3.61%	5.05%	1.16%

Table A.10: Variation of the assessed fatigue strengths for the octet EC under the 5 loading cases of Eq. (9) when the size of the extreme values population (5% of the nodes in Table 6) is decreased to 3% or increased to 7%.

Thin-walled Gyroid

% of EV	Tension (L_1) [MPa]	Torsion or pure shear (L_2) [MPa]	Combined tension and torsion with $\overline{\tau}_a = \overline{\sigma}_a$ (L_3) [MPa]	Combined tension and torsion with $\overline{\tau}_a = \frac{\overline{\sigma}_a}{3}$ (L_4) [MPa]	Combined tension and torsion with $\overline{\tau}_a = 3 \times \overline{\sigma}_a$ (L_5) [MPa]
3%	-1.84%	-15.45%	-3.25%	-5.48%	-5.22%
7%	3.13%	3.25%	3.25%	4.79%	2.61%

Table A.11: Variation of the assessed fatigue strengths for the thin-walled gyroid EC under the 5 loading cases of Eq. (9) when the size of the extreme values population (5% of the nodes in Table 6) is decreased to 3% or increased to 7%.

References

[1] S. Yavari, R. Wauthlé, J. Van der Stok, A. Riemslag, M. Janssen, M. Mulier, J. Kruth, J. Schrooten, H. Weinans, A. Zadpoor, Fatigue behavior of porous biomaterials manufactured using selective laser melting, Mater Sci Eng, C 33 (2013) 4849–4858.
URL https://doi.org/10.1016/j.msec.2013.08.006

[2] A. Zargarian, M. Esfahanian, J. Kadkhodapour, S. Ziaei-Rad, Numerical simulation of the fatigue behavior of additive manufactured titanium porous lattice structures, Mat Sci Eng, C 60 (2015) 339–347.
URL https://doi.org/10.1016/j.msec.2015.11.054

[3] M. Dallago, V. Fontanari, E. Torresani, M. Leoni, C. Pederzolli, C. Potrich, M. Benedetti, Fatigue and biological properties of Ti-6Al-4V ELI cellular structures with variously arranged cubic cells made by selective laser melting, J Mech Behav Biomed Mater 78 (2018) 381–394.
URL https://doi.org/10.1016/j.jmbbm.2017.11.044

[4] N. Hrabe, P. Heinl, B. Flinn, C. Koner, R. Bordia, Compression-compression fatigue of selective electron beam melted cellular titanium (Ti-6Al-4V), J Biomed Mater Res, B: Appl Biomater 99 (2) (2011) 313–320.
URL https://DOI:10.1002/jbm.b.31901

[5] M. Speirs, B. Van Hooreweder, J. Van Humbeeck, J. Kruth, Fatigue behaviour of NiTi shape memory alloy scaffolds produced by SLM, a unit cell design comparison, J Mech Behav Biomed Mater 70 (2017) 53–59.
URL https://doi.org/10.1016/j.jmbbm.2017.01.016

[6] B. Hooreweder, R. Boonen, D. Moens, J. Kruth, P. Sas, On the determination of fatigue properties of Ti6Al4V produced by Selective Laser Melting, 53rd AIAA/ASME/ASCE/AHS/ASC Structures, Structural Dynamics and Materials Conference. Honolulu, Hawaii, USA (2012).
URL https://doi.org/10.2514/6.2012-1733

[7] S. Liu, H. Du, Investigation on fatigue property of three-dimensional reticulated porous metal foams, J Mater Sci Technol 28 (5) (2012) 569–575.
URL https://doi.org/10.1179/1743284711Y.0000000111

[8] K. Chan, M. Koike, R. Mason, T. Okabe, Fatigue life of titanium alloys fabricated by additive layer manufacturing techniques for dental implants, Metall Mater Trans A 44 (2) (2013) 1010–1022.
URL https://doi.org/10.1007/s11661-012-1470-4

[9] S. Yue, R. Pillar, G. Weatherly, Fatigue strength of porous coated Ti-6Al-4V implant alloy, J Biomed Mater Res 18 (9) (1984) 1043–1058.
URL https://doi.org/10.1002/jbm.820180908

[10] M. Jamshidinia, F. Kong, R. Kovacevic, The numerical Modeling of Fatigue Properties of a Bio-Compatible Dental Implant Produced by Electron Beam Melting (EBM)®, Solid Freeform Fabrication Proceedings (2013) 12–14.

[11] P. Terriault, V. Brailovski, Modeling and simulation of large, conformal, porosity-graded and lightweight lattice structures made by additive manufacturing, J Mech

Behav Biomed Mater 138 (2018) 1–11.
URL https://doi.org/10.1016/j.finel.2017.09.005

[12] A. Yavari, S. Ahmadi, R. Wauthle, B. Pouran, J. Schrooten, H. Weinans, A. Zadpoor, Relationship between unit cell type and porosity and the fatigue behavior of selective laser melted meta-biomaterials, J Mech Behav Biomed Mater 43 (2015) 91–100.
URL https://doi.org/10.1016/j.jmbbm.2014.12.015

[13] S. Zhao, S. Li, W. Hou, Y. Hao, R. Yang, R. Misra, The influence of cell morphology on the compressive fatigue behavior of Ti-6Al-4V meshes fabricated by electron beam melting, J Mech Behav Biomed Mater 59 (2016) 251–264.
URL https://doi.org/10.1016/j.jmbbm.2016.01.034

[14] R. Hedayati, H. Hosseini-Toudeshky, M. Sadighi, M. Mohammadi-Aghdam, A. Zadpoor, Computational prediction of the fatigue behavior of additively manufactured porous metallic biomaterials, Int J Fatigue 84 (2016) 67–79.
URL https://doi.org/10.1016/j.ijfatigue.2015.11.017

[15] E. Barbero, Finite element analysis of composite materials, CRC Press, Taylor & Francis Group, 2007.

[16] M. Montemurro, A. Catapano, D. Doroszewski, A multi-scale approach for the simultaneous shape and material optimisation of sandwich panels with cellular core, Compos Part B-Eng 91 (2016) 458–472.
URL https://doi.org/10.1016/j.compositesb.2016.01.030

[17] L. Cappelli, M. Montemurro, F. Dau, L. Guillaumat, Characterisation of composite elastic properties by means of a multi-scale two-level inverse approach, Compos Struct 204 (2018) 767–777.
URL https://doi.org/10.1016/j.compstruct.2018.08.007

[18] K. Refai, M. Montemurro, C. Brugger, N. Saintier, Determination of the effective elastic properties of titanium lattice structures, Mech Adv Mater Struc (2019).
URL https://doi.org/10.1080/15376494.2018.1536816

[19] S. Kapfer, S. Hyde, K. Mecke, C. Arns, G. Schröder-Turk, Minimal surface scaffold designs for tissue engineering, Biomaterials 32 (29) (2011) 6875–6882.
URL https://doi.org/10.1016/j.biomaterials.2011.06.012

[20] A. Panesar, M. Abdi, D. Hickman, I. Ashcroft, Strategies for functionally graded lattice structures derived using topology optimisation for Additive Manufacturing, Addit Manuf 19 (2018) 81–94.
URL https://doi.org/10.1016/j.addma.2017.11.008

[21] M. Suard, G. Martin, P. Lhuissier, R. Dendievel, F. Vignat, J. Blandin, F. Villeneuve, Mechanical equivalent diameter of single struts for the stiffness prediction of lattice structures produced by Electron Beam Melting, Addit Manuf 8 (2015) 124–131.
URL https://doi.org/10.1016/j.addma.2015.10.002

[22] B. Vaysette, N. Saintier, C. Brugger, M. Elmay, Comportement en fatigue de pièces de Ti-6Al-4V obtenues par SLM et EBM : effet de la rugosité, Ph.D.thesis, Ecole Nationale Supérieure des Arts et Métiers ParisTech (2019).

[23] A. Charles, A. Elkaseer, L. Thijs, V. Hagenmeyer, S. Scholz, Effect of Process Parameters on the Generated Surface Roughness of Down-Facing Surfaces in Selective Laser Melting, Appl. Sci. 9 (6) (2019) 1256.
URL https://doi.org/10.3390/app9061256

[24] M. Simonelli, Y. Y. Tse, C. Truck, Effect of the build orientation on the mechanical properties and fracture modes of SLM Ti-6Al-4V, In : Materials Science and Engineering A 616 (2014) 1–11.

[25] G. Yoder, D. Eylon, On the effect of colony size on fatigue crack growth in Widmanstätten structure $\alpha+\beta$ titanium alloys, Metall Mater Trans A 10 (11) (1979) 1808–1810.
URL https://doi.org/10.1016/S0921-5093(01)01014-0

[26] B. Vayssette, N. Saintier, C. Brugger, M. Elmay, E. Pessard, Numerical modelling of surface roughness effect on the fatigue behavior of Ti-6Al-4V obtained by additive manufacturing, Int J Fatigue 123 (2019) 180–195.
URL https://doi.org/10.1016/j.ijfatigue.2019.02.014

[27] G. Bertolino, M. Montemurro, G. Pasquale, Multi-scale shape optimisation of lattice structures : an evolutionary-based approach, Int J Interact Des Manuf (2019).
URL https://doi.org/10.1007/s12008-019-00580-9

[28] A. Catapano, M. Montemurro, A multi-scale approach for the optimum design of sandwich plates with honeycomb core. Part I: Homogenisation of core properties, Compos Struct 118 (2014) 664–676.
URL https://doi.org/10.1016/j.compstruct.2014.07.057

[29] A. Catapano, M. Montemurro, A multi-scale approach for the optimum design of sandwich plates with honeycomb core. Part II: The optimisation strategy, Compos Struct 118 (2014) 677–690.
URL https://doi.org/10.1016/j.compstruct.2014.07.058

[30] L. Cappelli, M. Montemurro, F. Dau, L. Guillaumat, Multi-scale identification of the viscoelastic behaviour of composite materials through a non-destructive test, Mechanics of Materials (2019).
URL https://doi.org/10.1016/j.mechmat.2019.103137

[31] L. Cappelli, M. Montemurro, F. Dau, L. Guillaumat, Multi-scale identification of the elastic properties variability for composite materials through a hybrid optimisation strategy, Compos Part B-Eng (2019).
URL https://doi.org/10.1016/j.compositesb.2019.107193

[32] M. Montemurro, M. Izzi, J. El-Yagoubi, D. Fanteria, Least-weight composite plates with unconventional stacking sequences: Design, analysis and experiments, J Compos Mater (2019).
URL https://doi.org/10.1177/0021998318824783

[33] G. Pasquale, M. Montemurro, A. Catapano, G. Bertolino, L. Revelli, Cellular structures from additive processes: design, homogenization and experimental validation, Procedia Structural Integrity 8 (2018) 75–82.
URL https://doi.org/10.1016/j.prostr.2017.12.009

[34] M. Montemurro, A. Catapano, Chapter : A new paradigm for the optimum design of variable angle tow laminates, In : Variational analysis and aerospace engineering : mathematical challenges for the aerospace of the future. 1st Edition of Optimization and Its Applications, Springer International Publishing 116 (2016) 375–400.
URL http://dx.doi.org/10.1007/978-3-319-45680-5

[35] M. Montemurro, An extension of the Polar Method to the First-order Shear Deformation Theory of laminates, Compos Struct 127 (2015) 328–339.
URL https://doi.org/10.1016/j.compstruct.2015.03.025

[36] M. Delucia, A. Catapano, M. Montemurro, J. Pailhès, Determination of the effective thermoelastic properties of cork-based agglomerates, J Reinf Plast Comp 38 (16) (2019) 760–776.
URL https://doi.org/10.1177/0731684419846991

[37] B. Crossland, Effect of large hydrostatic pressures on the torsional fatigue strength of an alloy steel, Proceedings of the International Conference on Fatigue of Metals, Institution of Mechanical Engineers (1956) 138–149.

[38] G. Sines, Behavior of Metals under Complex Static and Alternating Stresses, In: Metal Fatigue, G. Sines and J.L. Waisman. Eds., McGraw Hill (1959) 145–169.

[39] K. Dang Van, I. Papadopoulos, High Cycle Metal Fatigue, From Theory to Applications, Springer Verlag, CISM courses and lectures (392) (1999).

[40] W. Findley, A Theory for the Effect of Mean Stress on Fatigue of Metals Under Combined Torsion and Axial Load or Bending, J Eng Ind 81 (4) (1959) 301–305.
URL https://doi.org/10.1115/1.4008327

[41] K. Matake, An explanation on Fatigue Limit under Combined Stress, Bulletin of the Japanese Society of Mechanical Engineers 20 (141) (1977) 257.
URL https://doi.org/10.1299/jsme1958.20.257

[42] C. Froustey, S. Lasserre, Multiaxial fatigue endurance of 30NCD16 steel, Int J Fatigue 11 (3) (1989) 169–175.
URL https://doi.org/10.1016/0142-1123(89)90436-2

[43] N. Saintier, T. Palin-luc, J. Benabes, F. Cocheteux, Non-local energy based fatigue life calculation method under multiaxial variable amplitude loadings, Int J Fatigue 54 (2013) 68–83.
URL https://doi.org/10.1016/j.ijfatigue.2012.12.013

[44] T. Palin-Luc, S. Lasserre, An energy based criterion for high cycle multiaxial fatigue, Eur.J.Mech. A/Solids 17 (2) (1998) 237–251.
URL https://doi.org/10.1016/S0997-7538(98)80084-3

[45] A. Banvillet, T. Palin-Luc, S. Lasserre, A volumetric energy based high cycle multiaxial fatigue citerion, Int J Fatigue 25 (8) (2003) 755–769.
URL https://doi.org/10.1016/S0142-1123(03)00048-3

[46] B. Vayssette, N. Saintier, C. Brugger, M. Elmay, E. Pessard, Surface roughness of Ti-6Al-4V parts obtained by SLM and EBM: Effect on the High Cycle Fatigue life, Procedia Engineering 213 (2018) 89–97.
URL https://doi.org/10.1016/j.proeng.2018.02.010

[47] R. Fisher, The Genetical Theory of Natural Selection, Oxford University Press, 1930. URL http://dx.doi.org/10.5962/bhl.title.27468

[48] A. Jenkinson, The frequency distribution of the annual maxima (or minimum) values of meteorological elements, Quart J Roy Meteorol Soc 81 (1955) 158–171. URL https://doi.org/10.1002/qj.49708134804